ACS OMEGA

Open Access

http://pubs.acs.org/journal/acsodf

Article

Enhancing the Performance of Lithium−Oxygen Batteries with Quasi-Solid Polymer Electrolytes

SiXin Jia, FengQuan Liu,* JinXin Xue, Rui Wang, Hong Huo, JianJun Zhou,* and Lin Li*

Cite This: *ACS Omega* 2023, 8, 36710−36719

Read Online

ACCESS | Metrics & More | Article Recommendations | Supporting Information

ABSTRACT: The quasi-solid electrolyte membranes (QSEs) are obtained by solidifying the precursor of unsaturated polyester and liquid electrolyte in a glass fiber. By modifying the ratio of tetraethylene glycol dimethyl ether, QSE with balanced ionic conductivity, flexibility, and electrochemical stability window is acquired, which is helpful for inhibiting the decomposition of electrolyte on the cathode surface. The QSE is beneficial to the interfacial reaction of Li^+, electrons, and O_2 in the quasi-solid lithium−oxygen battery (LOB), can reduce the crossover of oxygen to the anode, and extend the cycle life of LOBs to 317 cycles. Benefitting from the application of QSE, a more stable solid electrolyte interface layer can be constructed on the anode side, which can homogenize Li^+ flux and facilitate uniform Li deposition. Lithium−oxygen pouch cell with in situ formed QSE_2 works well when the cell is folded or a corner is cut off. Our results indicate that the QSE plays important roles in both the cathode and Li metal anode, which can be further improved with the in situ forming strategy.

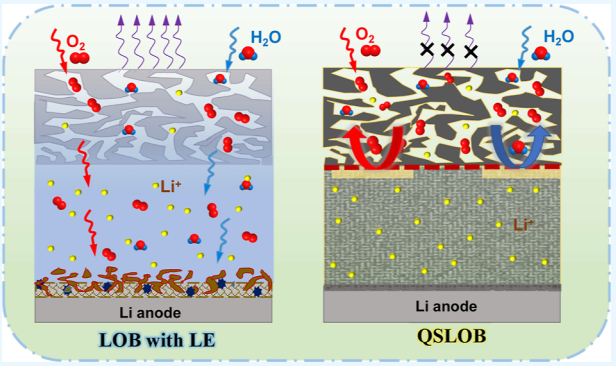

1. INTRODUCTION

In recent years, more and more attention has been paid to the safe battery system with higher energy density.[1−3] Metallic lithium (Li) has high theoretical capacity (3860 mA h g^{-1}) and low oxidation−reduction potential (−3.040 V *vs* standard hydrogen electrode), which has been known as the "Holy Grail" for higher energy-density batteries.[4] Lithium−oxygen batteries (LOBs), with metallic Li as the anode and O_2 as the cathode, has a very high theoretical energy density of about 3500 W h kg^{-1}, and thus is one of the most promising next-generation battery systems.[5−7] However, the discharge product Li_2O_2 in the cathode side is insulated and insoluble, leading to large charge overpotential, which causes the decomposition of liquid electrolyte (LE).[8−11] In the anode side, Li metal has very high reactivity, consuming LE continuously and resulting in a thick solid electrolyte interface (SEI) layer and large polarization.[12] Furthermore, the volatilization and leakage of LE in the semiopen LOBs is also a big challenge.[13,14] To address the problems related to LE, a quasi-solid electrolyte (QSE) might be a good choice because it can provide high ionic conductivity comparable to LE, good flexibility, and can reduce leakage and the crossover of oxygen to the anode.[15−17]

Gel polymer electrolyte (GPE) is a kind of the most studied QSEs with a polymer matrix plasticized by the aprotic electrolyte, which has both excellent mechanical properties of polymer matrix and high ionic conductivity of LE.[18,19] Many GPEs have been reported in lithium-ion batteries with polymer matrices, such as poly(ethylene oxide),[20,21] polyvinylidene difluoride (PVDF),[22,23] polyacrylonitrile,[24,25] poly(methyl methacrylate),[26,27] etc. However, the GPEs used in lithium-ion batteries can run only a few cycles in LOBs due to using an ester solvent (ethylene carbonate, propylene carbonate, etc.)[28] because the decomposition of electrolyte was considered to be the dominant process during battery cycling.[29,30] PVDF-based QSE with tetraethylene glycol dimethyl ether (TEGDME) as a plasticizer has showed much improved performance in LOB.[31] By combining nano-SiO_2 in the PVDF matrix, a super-hydrophobic QSE was reported to further prevent the crossover of O_2 and H_2O to the Li anode.[32] Other QSEs, such as cross-linked poly(ethylene glycol) methyl ether methacrylate and SiO_2,[33] LE-plasticized SiO_2-filled thermoplastic polyurethane matrix,[34] dimethyl sulfoxide-plasticized polyetheretherketone, and dextrin nanosponge matrix,[35] ethoxylated trimethylolpropanetriacrylate-plasticized PVDF-HFP matrix,[36] etc. were also reported, which have showed the capability of inhibiting Li dendritic deposition and preventing O_2 crossover in LOBs. Recently, we synthesized a unsaturated polyester, which has been used to prepare polymer electrolyte membranes with high ionic conductivity (1.99×10^{-3} S cm^{-1} at 30 °C) and low glass transition temperature

Received: April 28, 2023
Accepted: September 14, 2023
Published: September 25, 2023

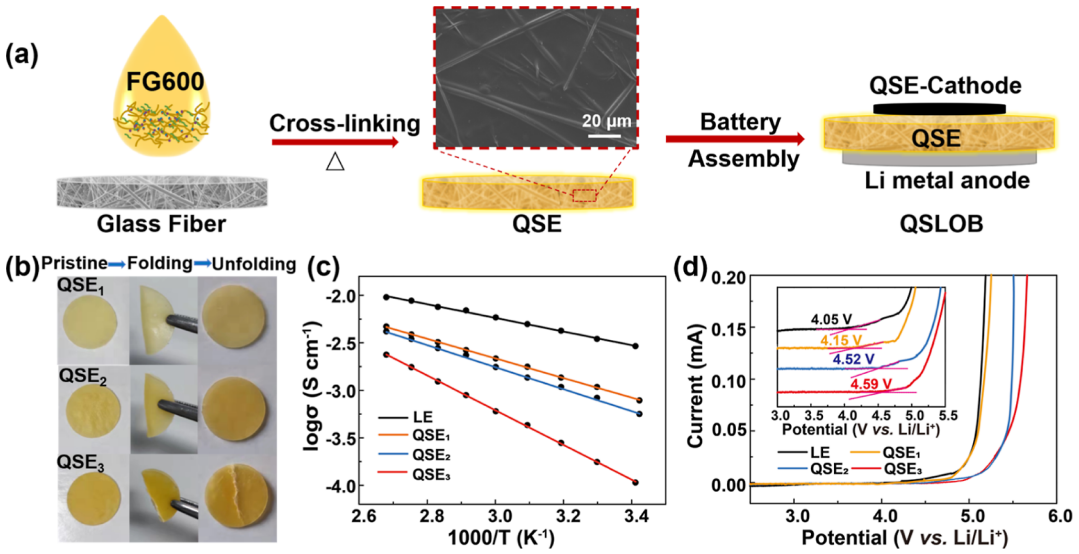

Figure 1. (a) Schematic illustration of preparing the QSE and QSLOB. (b) Photographs of QSE membranes. (c) Temperature dependence of ionic conductivity for LE, QSE_1, QSE_2, and QSE_3 at the temperature range of 20−100 °C. (d) LSV curves of LE, QSE_1, QSE_2, and QSE_3.

(−54.2 °C).[37] It is expected that the polymer electrolyte can improve the cycle performance of LOBs.

Herein, QSEs with a glass fiber (GF) membrane as the matrix were prepared by a cross-linked unsaturated polyester precursor. By adjusting the ratio of polyester to plasticizer, we acquired the QSE with both good flexibility and electrochemical properties. When applied in LOBs, QSEs have showed excellent compatibility with a Li metal anode, which can promote uniform Li plating/stripping by homogenizing Li^+ flux. The QSE is beneficial to the interfacial reaction of Li^+, electrons, and O_2 and can extend the cycle life of LOBs to 317 cycles with a curtailed capacity of 500 mA h g^{-1} at 200 mA g^{-1}.

2. EXPERIMENTAL SECTION

2.1. Synthesis of Unsaturated Polyesters. Unsaturated polyester FG600 was synthesized according to ref 37. Typically, fumaric acid (0.133 mol, 15.4 g) and polyethylene glycol (M_w = 600) (0.146 mol, 87.6 g) were added into the reaction flask, which was first heated to 90 °C with mechanical stirring under a N_2 atmosphere. The temperature was raised slowly to 195 °C at a heating rate of 1 °C min^{-1}, held for 0.5 h, then raised to 220 °C, and maintained for 2 h. After that, tetrabutyl titanate was added as a catalyst to accelerate the esterification reaction. The reaction continued for another 0.5 h and then vacuumized for about 10 min. The raw product was dissolved overnight with chloroform and then precipitated with a large amount of anhydrous ethanol. After rotary evaporating and vacuum drying at 50 °C, the unsaturated polyester FG600 was obtained.

2.2. Preparation of QSE. QSE was prepared by a cross-linked precursor solution in a GF membrane at 90 °C, which consisted of benzoyl peroxide (BPO), lithium bis(trifluoromethanesulfonyl) imide (LiTFSI), unsaturated polyester (FG600), and TEGDME. BPO was used as an initiator with a ratio of 2% to the mass of FG600, the mole ratio of ethylene oxide/Li was 6:1, and TEGDME was used as a plasticizer. QSE_1, QSE_2, and QSE_3 meant that the mass ratios of FG600 to TEGDME were 1:4, 1:2, and 1:1, respectively.

2.3. Preparation of Cathode. Ru-MOF (metal−organic framework) was used as a catalyst for the oxygen reduction reaction and oxygen evolution reaction due to staggered porous tunnels and abundant active sites, which was prepared according to ref 38. $RuCl_3{\cdot}nH_2O$ and 1,3,5-benzenetricarboxylic acid were dissolved in a mixed solvent of acetic acid and deionized water at a molar ratio of 3:2, where the volume ratio of acetic acid to water was 1:5. The solution was placed in a hydrothermal synthesis reactor and reacted at 160 °C for 3 days, which was filtered off and washed with deionized water. The solid crude product was freeze-dried overnight to obtain Ru-MOFs. The characterization of the Ru-MOF catalyst can be seen in Figure S1. Second, carbon nanotubes (CNTs) were purified by acid treatment. After soaking in concentrated nitric acid overnight, the CNTs were washed with a large amount of deionized water to neutral and dried. Third, cathode slurry was prepared by grinding the Ru-MOF, CNTs, and binder (PVDF or QSE_2) at a mass ratio of 45:45:10 with NMP as a solvent. The QSE cathode was prepared by coating the slurry on carbon paper with QSE_2 as a binder, and the common cathode was prepared with PVDF as a binder. After being dried overnight at 120 °C, the cathode was cut into discs with a diameter of 10 mm.

2.4. Physical Characterization. The structure was characterized by ^1H NMR (JNM-ECZ600R). The morphologies and elemental mapping were characterized by field-emission scanning electron microscopy (SEM, SU-8010, Hitachi) with energy-dispersive X-ray spectroscopy (EDS, XFlash6160, Bruker). The thermal behavior was studied by a differential scanning calorimeter (PerkinElmer DSC8000) in a temperature range from −70 to 100 °C with a heating rate of 10 K min^{-1} under a N_2 atmosphere. The thermal stability of QSEs was investigated by thermogravimetric analysis (TGA) with a thermal analysis instrument (STA449 F5) at a heating rate of 10 K min^{-1} under a N_2 atmosphere in a temperature range from 50 to 650 °C. Fourier transform infrared spectroscopy (FTIR) (Bruker VERTEX 70) was used to study functional groups of the products. The Raman measurement was conducted on a LABRAM ARAMIS spectrometer at 25 °C. Powder X-ray diffraction (XRD) was conducted on a Phillips X'pert Pro MPD diffractometer with Cu Kα (λ = 0.15418 nm). UV−vis spectra were performed with a Cary 60 UV−vis spectrometer (Agilent Technologies).

https://doi.org/10.1021/acsomega.3c02917
ACS Omega 2023, 8, 36710−36719

The discharge products on the surface of cathode were analyzed with X-ray photoelectron spectroscopy (XPS, ESCALAB 250 Xi).

2.5. Assembly of Li−O_2 Cell and Pouch Cell. Li metal anode (15.6 mm in diameter), QSE_s membrane, and the as-prepared QSE cathode were used to assemble Li|QSE_s|O_2 coin cells in an argon-filled glovebox (H_2O < 0.1 ppm, O_2 < 0.1 ppm). QSE_2@Li was prepared by coating QSE_2 on a Li foil. For comparison, Li|LE|O_2 and QSE_2@Li|LE|O_2 coin cells were also assembled with PVDF as the binder in the cathode. The LE is 1.0 M LiTFSI in TEGDME. QSLOBs with in situ formed QSE_2 were also assembled. When the GF membrane was soaked with precursor solution, it was placed between the cathode and Li anode. After sealed, the cells were heated at 90 °C to cross-link and in situ form QSE_2 in the cells. The Li−O_2 pouch cells with in situ formed QSE_2 were assembled using a precursor solution-soaked GF membrane, which were heated at 90 °C to cross-link and in situ form QSE_2 in the cell. One cathode with a size of 2.5 cm × 3.0 cm was coupled with two pieces of Li anode. The cell cores were packaged in an aluminum−plastic bag with holes on one side.

2.6. Electrochemical Characterization. The electrochemical impedance spectroscopy (EIS) was measured at a frequency range of 10^6 to 10^{-1} Hz using an electrochemical workstation (Interface 1010E, Gamry) at 25 °C. The Li^+ transference number (t_{Li}^+) was calculated by chronoamperometry with a DC potential of 10 mV, and EIS tests using an electrochemical workstation (interface 1010E, Gamry) at 25 °C. The electrochemical stability window was characterized by linear sweep voltammetry (LSV) at 25 °C and a scan rate of 0.1 mV s^{-1}. The cyclic voltammetry (CV) measurements were carried out at 2.0−4.5 V and a scan rate of 0.1 mV s^{-1}. Li−Li symmetric cells with LE were assembled with QSE_2@Li or Li as electrodes, separated by GF, and cycled at 0.5 mA cm^{-2} and 1.0 mA h cm^{-2}. The LOBs were cycled on a cell testing system (CT2001A LANHE, Wuhan Land Electronics Co., Ltd., China), and the purity and pressure of oxygen were 99.99% and 0.01 MPa, respectively. The mass loading of CNTs was about 0.3 mg cm^{-2}.

3. RESULTS AND DISCUSSION

Figure 1a shows the procedure of preparing the QSE membrane and QSLOB. The QSEs were prepared by filling the precursor mixture into the GF membrane, cross-linking, and vacuum drying. The precursor solution consisted of FG600, lithium salt, and TEGDME. Compared with the fibrillar and porous GF membrane, the surface of QSE shows a dense and relatively smooth morphology with a little glass fiber on its surface. The dense structure of QSE membrane is beneficial for preventing O_2 crossover and its corrosion on the Li metal anode.[26] The unsaturated polyester, FG600, was characterized by a ^{1}H NMR spectrum (Figure S2). The peak (*a*) at 6.86 ppm corresponds to the chemical shift of the hydrogen atom on the carbon−carbon double bond. The peak (*b*) at 4.32 ppm belongs to the chemical shift of hydrogen atom on the carbon linked to oxygen of the ester group, and the peak (*c*) at 3.71 ppm is assigned to the chemical shift of the hydrogen atom on the carbon linked to oxygen of the ether group. The peak (*d*) at 3.60 ppm is the chemical shift of the hydrogen atom on the carbon of the repeating unit of PEG. The large number of ether bonds in the FG600 backbone is helpful for endowing QSE with high ionic conductivity.

Three kinds of QSEs were prepared. QSE_1, QSE_2, and QSE_3 mean that the mass ratios of FG600 to TEGDME in the precursor mixture are 1:4, 1:2, and 1:1, respectively. As shown in Figure 1b, when folding the QSEs, QSE_3 cracks, while no crease is observed in QSE_1 and QSE_2, indicating that increasing the TEGDME content can improve their flexibility. Figure S3 shows the XRD profile of a QSE_2 membrane. Only a dispersing peak attributed to the diffraction of the amorphous part is observed at about 23°, indicating that the QSE_2 membrane is amorphous at room temperature. DSC was used to analyze the thermal behavior of the QSE materials. As shown in Figure S4, FG600 has a melting peak at 17.5 °C. While no melting peaks are observed in the range of −70 to 100 °C for cross-linked FG600 and QSE_2 samples, suggesting that cross-linking has successfully inhibited the crystallization of FG600 chain segments. The glass transition temperatures (T_g) of cross-linked FG600 and QSE_2 are −31.1 and −50.5 °C, respectively. Smaller T_g is observed in QSE_2 indicating that the TEGDME in QSE_2 has promoted the mobility of the chain segments. Because Li^+ transport is realized by complexing−decomplexing with ether oxygen groups in the amorphous chain segments, the amorphous nature and the relatively low T_g of QSE_2 are conducive to the migration of Li^+, which is beneficial to relatively high ionic conductivity.

As shown in Figure S5, the t_{Li}^+ of LE, QSE_1, QSE_2, and QSE_3 are determined through DC polarization and EIS measurements, which are 0.19, 0.62, 0.70, and 0.66, respectively. The t_{Li}^+ of QSEs are much larger than that of LE, indicating that the cross-linked polymer matrix can slow the transport of $TFSI^-$, reduce the effects of the concentration gradient, which is beneficial for mitigating the interface polarization, and delay the growth of Li dendrites. The addition of carbonyl groups in QSE_2 could promote the decoupling of ion pairs (Figure S6), which can further facilitate the movement of Li^+ inside the polymer matrix leading to the higher t_{Li}^+.

The ionic conductivity of QSEs was characterized by EIS, as shown in Figure 1c. At 20 °C, the ionic conductivities of LE, QSE_1, QSE_2, and QSE_3 are 2.91 × 10^{-3}, 7.83 × 10^{-4}, 5.64 × 10^{-4}, and 1.07 × 10^{-4} S cm^{-1}, respectively. Compared with LE, the ionic conductivity of QSEs gradually declines with a decrease in TEGDME content. The ionic conductivities of both LE and QSEs increase with an increase of temperatures. The Arrhenius equation was used to describe the conductivity−temperature behavior, and good linearity is observed after fitting. The activation energy (E_a) of LE, QSE_1, QSE_2 and QSE_3 are 0.06, 0.18, 0.20, and 0.39 eV, respectively. E_a of LE is much smaller than those of QSEs, implying the different way of Li^+ transport. In QSEs, Li^+ transport is realized by the coordination motion of both solvent and chain segments, so much larger E_a is needed. The higher the content of TEGDME, the lower the E_a, suggesting that the plasticizer can promote the motion of chain segments, decreasing the E_a of ion transport.

The electrochemical stability window was characterized by LSV, as shown in Figure 1d. The decomposition voltages of LE and QSEs are 4.05, 4.15, 4.51, and 4.59 V, respectively. LE has the lowest decomposition voltage. The decomposition voltage of QSEs increases with the decrease of the liquid component. The increased decomposition voltage may benefit from the confinement of the cross-linked polymer framework on the liquid component, which can reduce the probability of TEGDME encountering oxidation. Compared with the other

https://doi.org/10.1021/acsomega.3c02917
ACS Omega 2023, 8, 36710−36719

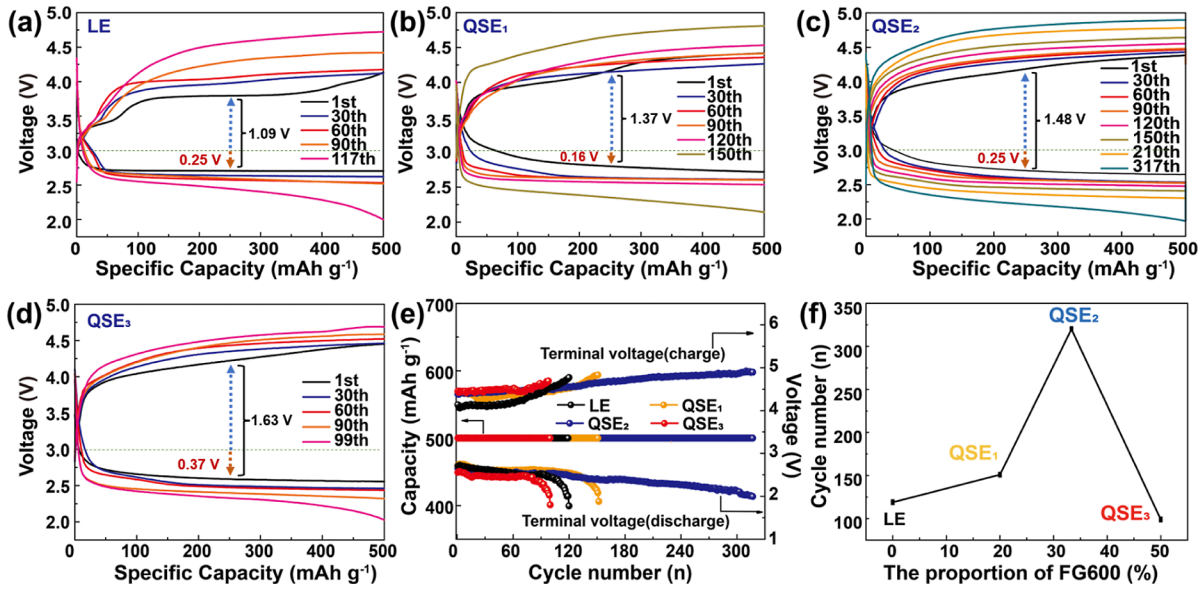

Figure 2. Selected discharge−charge curves of (a) Li|LE|O_2 batteries, (b) Li|QSE$_1$|O_2 batteries, (c) Li|QSE$_2$|O_2 batteries, and (d) Li|QSE$_3$|O_2 batteries. (e) Corresponding cycle performance with a curtailed capacity of 500 mA h g^{-1} at 200 mA g^{-1}. (f) Cycle lives of LOBs.

polymer electrolytes reported in the literature (Table S1), QSE$_2$ has relatively excellent electrochemical performance. Thermal stability of QSEs was determined by TGA, as shown in Figure S7. The QSEs are stable up to about 200 °C. Due to the presence of cross-linked polymer network in the QSEs, their initial decomposition temperatures are improved slightly compared with that of LE.

QSLOBs were assembled with QSE membranes and QSE cathode, as shown in Figure 1a. Control LOBs filled with LE were also assembled with PVDF as a binder. When a QSLOB and a control LOB contact a paper with the cathode side for a while, the control LOB will wet the paper while the QSLOB shows no sign of leakage (Figure S8). From the weight change over time of the assembled Li|LE|O_2 battery and Li|QSE$_2$|O_2 battery under negative pressure (Figure S9), it is clear that our QSLOB can mitigate the leakage of electrolyte.

Cycle performance of LOBs is shown in Figure 2. Compared with QSLOBs, the Li|LE|O_2 battery has the lowest polarization voltage of 1.09 V in the initial cycle due to the highest ionic conductivity. With the increase of the cycle number, the charge overpotential increases rapidly, especially after 60 cycles. The discharge voltage decreases sharply after 90 cycles and reaches the terminal voltage (2.0 V) at 117 cycles. The limited cycle numbers and rapid failure of the capacity are mainly due to the growth of Li dendrite, the generation of dead Li, incomplete decomposition of Li_2O_2 on the cathode, and high oxygen cross-contamination on the Li anode, leading to more side effects, especial the electrolyte decomposition.[39] When QSE$_s$ were used, the discharge curves of Li|QSE$_s$|O_2 batteries are oblique lines, different from that of Li|LE|O_2 batteries, which may be mainly attributed to different Li_2O_2 growth models. There are two Li_2O_2 growth models reported in the literature. In the solution model of Li_2O_2 in Li|LE|O_2 batteries, Li_2O_2 toroid grows in solution by disproportionation of soluble intermediate LiO_2, but the bigger size of insulating Li_2O_2 will lead to a higher charge overpotential.[40,41] While in the surface model, the Li_2O_2 film is coated on the cathode by the main electrochemical reaction of LiO_2 on the surface, which is easier to react due to the close contact with the cathode.[42,43] The oblique discharge curves of Li|QSE$_s$|O_2 batteries may indicate that the growth of the Li_2O_2 film follows the surface model. Both the initial discharge and charge overpotential of QSLOBs rise with the decrease of TEGDME in QSEs due to the decreased ionic conductivity (Figure 2b−e). The performance of QSLOBs is affected by the QSEs. As shown in Figure 2f, the Li|QSE$_1$|O_2, Li|QSE$_2$|O_2 and Li|QSE$_3$|O_2 batteries can run 150, 317, and 99 cycles, respectively. The Li|QSE$_2$|O_2 has the longest cycle life, while the life of Li|QSE$_3$|O_2 is the shortest. The lives of LOBs increase first and then decrease with the reduction of TEGDME ratio in the electrolyte, which may have been affected by the number of triple-phase boundaries (TPBs) for the reaction of Li^+, electrons, and O_2.[44−46] Compared LE with QSEs, the TPBs should increase with the decrease of TEGDME content because the less liquid exponent, the more chance electrode material is exposed to oxygen. Therefore, the cycle lives of batteries increase with the reduction of TEGDME in the electrolyte first. In the Li|QSE$_2$|O_2 batteries, the most balanced TPBs and ionic conductivity may have been attained, so the life is the longest, showing a splendid cycle performance as compared with those reported in the literature (Table S1). Although the greatest number of TPBs may exist in the Li|QSE$_3$|O_2 batteries, the life of the Li|QSE$_3$|O_2 batteries is the shortest, which may be attributed to the lowest ionic conductivity of QSE$_3$. The low ionic conductivity of QSE$_3$ has resulted in too large polarization, as shown in Figure 2d, deteriorating the battery performance.

As shown in Figure 2a−d, the initial polarization voltage is the smallest in Li|LE|O_2 batteries, and the highest in Li|QSE$_3$|O_2 batteries, which rises fast with cycle numbers. The discharge and charge voltages at the end of each cycle ascend at a much lower rate in Li|QSE$_1$|O_2 and Li|QSE$_2$|O_2 (Figure 2e). EIS was used to characterize the internal resistance variation during cycling, which was fitted with an equivalent circuit model, as shown in the inset of Figure S10. R_b, the bulk resistance, increases with the decrease of TEGDME ratio in the electrolyte (Figure S11a), showing the same trend of ionic conductivity at 20 °C (Figure 1c), which indicates that R_b is directly affected by the ionic conductivity. R_{SEI}, the resistance

https://doi.org/10.1021/acsomega.3c02917
ACS Omega 2023, 8, 36710−36719

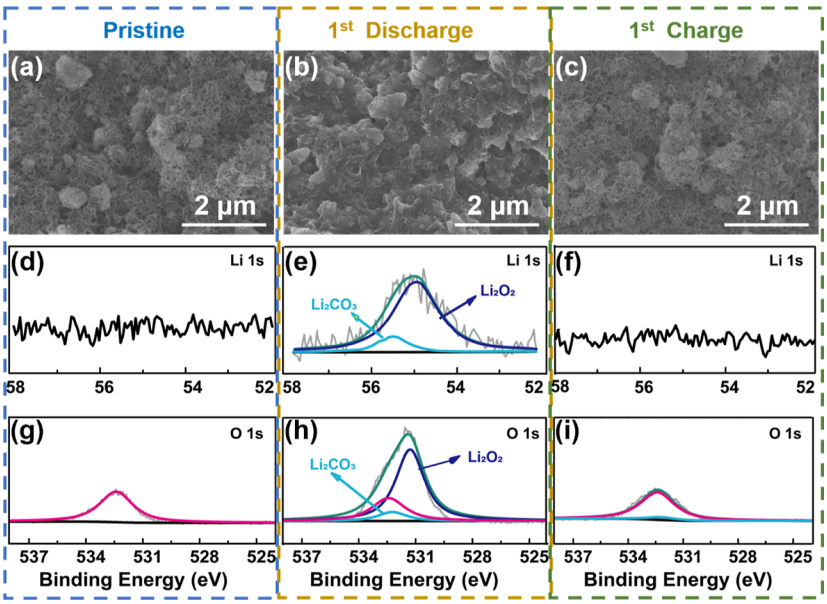

Figure 3. Characterizing discharge products on cathodes of Li|QSE$_2$|O$_2$ batteries. SEM images of (a) pristine, after the first (b) discharge and (c) charge cycle. Li 1s XPS profiles of (d) pristine, after the first (e) discharge and (f) charge cycles. O 1s XPS profiles of (g) pristine, after the first (h) discharge and (i) charge cycles.

at the solid electrolyte interface, decreases first and then increases with the cycle numbers (Figure S11b). The R_{SEI} in the Li|QSE$_3$|O$_2$ battery increases abruptly after 10 cycles, which may be attributed to the large space charge at the interface due to low ionic conductivity of QSE$_3$. After 50 cycles, R_{SEI} in Li|QSE$_1$|O$_2$ begins to increase. 70 cycles later, R_{SEI} in Li|QSE$_2$|O$_2$ is the smallest. In Li−O$_2$ batteries, R_{SEI} mainly originate from space charge at the interface, the irreversible discharge product on the cathode and the decomposition of carbon nanotube, binder, LiTFSI and TEGDME on the interface of cathode,[47,48] as well as the accumulated SEI layer formed by the reaction of metallic Li with liquid exponents on the interface of anode side.[49,50] The smallest R_{SEI} increase in Li|QSE$_2$|O$_2$ indicates that QSE$_2$ may be helpful for promoting the formation of a stable interface layer on the electrodes. R_{ct} increases with the decrease of the TEGDME ratio (Figure S11c), suggesting that the plasticizer can promote the reaction kinetics.

The morphologies of discharged and charged cathodes of Li|QSE$_2$|O$_2$ and Li|LE|O$_2$ batteries were observed by SEM, as shown in Figures 3a−c and S12. The pristine cathodes show a porous structure (Figure 3a and S12a). After the first discharge, the cathode of Li|QSE$_2$|O$_2$ batteries is covered uniformly by the film-like discharge products (Figure 3b), while the toroid-like discharge products are observed in the cathode of Li|LE|O$_2$ batteries (Figure S12b). In the subsequent charge cycle, the discharge products completely disappear and the cathode almost restores to its original morphology, indicating the good reversibility of the LOBs (Figure 3c and Figure S12c).[51−53] XRD profiles and UV−vis spectroscopy of the cathodes after discharge and charge can verify the reversible formation and decomposition of Li$_2$O$_2$ (Figures S13, S14). XPS spectra of Li 1s and O 1s were further used to characterize the discharge and charge products, as shown in Figure 3d−i. No Li 1s peak is observed in the pristine cathode, as shown in Figure 3d. After the first discharge, a broad peak that can be split into two peaks at ∼55.0 and 55.5 eV is observed, attributed to the formation of Li$_2$O$_2$ and Li$_2$CO$_3$,[54] and the latter is due to oxidized CNTs or TEGDME irreversibly (Figure 3e).[55,56] After the first charge, the peaks disappear, indicating that the reaction is reversible (Figure 3f). Meanwhile, in the O 1s profile, a new peak at 531.2 eV is observed in the first discharge cycle (Figure 3g,h), which also disappears after the first charge cycle (Figure 3i), verifying the formation and decomposition of Li$_2$O$_2$.

XPS spectra of Li 1s and O 1s after 50 cycles are shown in Figure 4. Compared with the cathode after the first charge, a new peak appears in the profiles of Li 1s after the 50th charge. The Li 1s peak can be split into two peaks at 56.2 and 55.5 eV, assigned to LiF and Li$_2$CO$_3$. The intensities of the Li 1s peaks in the Li|QSE$_2$|O$_2$ battery are much smaller than those in Li|LE|O$_2$ batteries, suggesting less Li remnants in the cathode after 50 cycles. Meanwhile, in O 1s profiles, the intensity of X-ray spectroscopy of O 1s attributed to the formation of Li$_2$CO$_3$ is much smaller in Li|QSE$_2$|O$_2$ than that in Li|LE|O$_2$ batteries. The new peak at 533.7 eV in O 1s represents the various

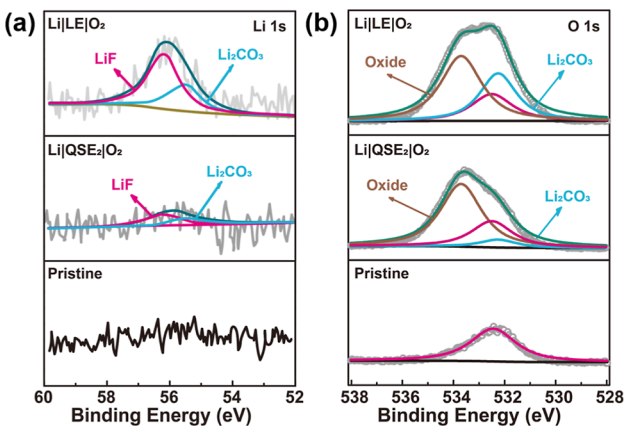

Figure 4. XPS spectra of pristine and charged cathode (after the 50th cycle) from Li|LE|O$_2$ and Li|QSE$_2$|O$_2$ batteries. XPS profiles of (a) Li 1s and (b) O 1s.

https://doi.org/10.1021/acsomega.3c02917
ACS Omega 2023, 8, 36710−36719

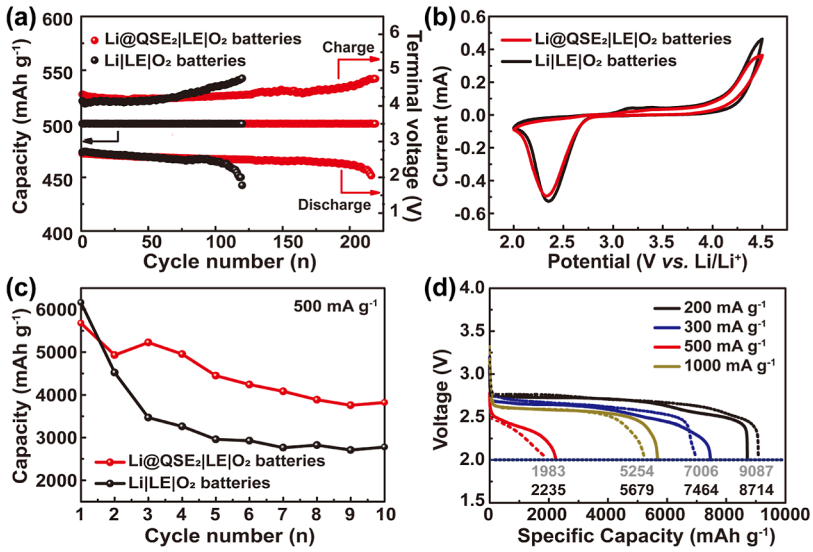

Figure 5. Cycle performance of Li|LE|O_2 and Li@QSE_2|LE|O_2 batteries. (a) Capacity attenuation at 500 mA h g^{-1} and 200 mA g^{-1}. (b) CV profiles under an O_2 atmosphere. (c) Full discharge capacity of Li|LE|O_2 and Li@QSE_2|LE|O_2 batteries at 500 mA g^{-1}. (d) Galvanostatic discharge profiles of the Li@QSE_2|LE|O_2 batteries (solid lines) and Li|LE|O_2 batteries (dashed lines).

byproducts that occur during cycling. It is well known that during cycling, the decomposition of LiTFSI, TEGDME, as well as QSE_2 etc. will generate byproducts, such as LiF, Li_2CO_3, other ether, as well as ester etc. on the cathode.[49,57] Less byproducts accumulated indicate that QSE_2 has inhibited the decomposition of electrolyte on the cathode, which is helpful for retarding the growth of overpotential and prolonging the cycle life of LOBs.

In the anode side of LOBs, the main contribution to R_{SEI} originated from the interface layer formed by the reaction of freshly deposited and highly active Li with the electrolyte, as well as Li metal anode corrosion caused by O_2 and H_2O.[58,59] The H-type permeation experiment (Figure S15) verifies that the QSE_2 membrane can resist the permeation of H_2O. The formation of LiOH is an indication of Li foil being corroded by O_2 and H_2O. XRD analysis shows less signal of LiOH on the Li anode from the Li|QSE_2|O_2 battery (Figure S16), which demonstrates the great advantage of QSE_2 in mitigating the crossover of the O_2 and H_2O to the Li anode.

The smallest R_{SEI} in Li|QSE_2|O_2 may imply that QSE_2 has promoted the formation of a more stable interfacial layer on the Li metal anode. To explore the possible effect of QSEs on protecting the Li metal anode, QSE_2 was coated on Li foil to prepare Li@QSE_2. The surface of Li@QSE_2 has a uniform slightly wrinkled coat with a thickness of about 35 μm (Figure S17). When Li@QSE_2 was used to assemble Li−Li symmetric cells, Li is uniformly plated, stripped, and the cells can show very stable cycle performance (Figure S18, S19b,d). In contrary, an obvious overpotential hysteresis occurs in the Li|LE|Li cells after about 100 h, which may originate from the growth of Li dendrites and the continuous reaction of freshly deposited Li dendrites with electrolytes (Figure S19 a,c), resulting in gradually increased thickness of SEI layer and internal resistance.[60] Much more stable cycle performance of the Li@QSE_2|LE|QSE_2@Li cell suggests that the QSE_2 coat is beneficial to forming a more stable interface layer on the surface of Li electrodes.

Li@QSE_2 was further used to assemble the Li@QSE_2|LE|O_2 batteries. Long-term cycle performance of Li@QSE_2|LE|O_2 batteries is shown in Figure 5a. Although the Li@QSE_2|LE|O_2 battery has a higher charge terminal voltage at first, it increases much more slowly than that in the Li|LE|O_2 battery. The Li@QSE_2|LE|O_2 and Li|LE|O_2 batteries can run 217 and 120 cycles, respectively. The Li−O_2 batteries with a curtailed capacity of 1000 mA h g^{-1} were also cycled (Figure S20). The cycle life doubles, showing the obvious advantage of Li@QSE_2|LE|O_2 over Li|LE|O_2 batteries. Because the only difference is the QSE_2 coat on the Li foil surface, the performance improvement should originate from the protection of QSE_2 on the Li metal anode. CV of the Li@QSE_2|LE|O_2 batteries has demonstrated that the presence of QSE_2 on Li foil has not brought other side reactions (Figure 5b and S21). The Li@QSE_2|LE|O_2 battery has a full discharge capacity of 5679.4 mA h g^{-1} at a current density of 500 mA g^{-1}, slightly lower than that of the Li|LE|O_2 battery (Figure 5c and S22). However, the discharge capacity of the Li@QSE_2|LE|O_2 battery decays at a much slow rate. After 10 cycles, the capacity of the Li@QSE_2|LE|O_2 battery is 3820.6 mA h g^{-1}, much higher than that of the Li|LE|O_2 battery (2778.4 mA h g^{-1}). Figure 5d shows the rate performance of Li@QSE_2|LE|O_2 and Li|LE|O_2 batteries. As current densities increasing from 100 to 1000 mA g^{-1}, the Li@QSE_2|LE|O_2 battery can discharge 8714 and 2235 mA h g^{-1}, respectively, which shows a better rate performance than the Li|LE|O_2 battery, especially at high current densities. EIS results have showed that although larger initial internal resistance exists in Li@QSE_2|LE|O_2 batteries, R_{SEI} and R_{ct} decrease from the 10th to 50th cycles, while the opposite trend is observed in the Li|LE|O_2 battery, which further demonstrates that QSE_2 can stabilize the Li anode interface, prevent corrosion of LE on the Li metal anode and alleviate its consumption (Figure S23 and Table S2). Porous deposition layer is observed on the Li anode of the Li|LE|O_2 battery (Figure 6a,c), while much denser and thinner deposition is seen on the Li anode of the Li@QSE_2|LE|O_2 battery (Figure 6b and S24a,b). The surface of the Li anode is covered by QSE_2, and no Li dendrites but some GF are observed on the surface (Figure 6d). It can be deduced that the QSE_2 may have contributed to constructing a more stable interface layer on the Li metal anode by homogenizing the Li^+ flux to promote uniform Li deposition and stripping.

https://doi.org/10.1021/acsomega.3c02917
ACS Omega 2023, 8, 36710−36719

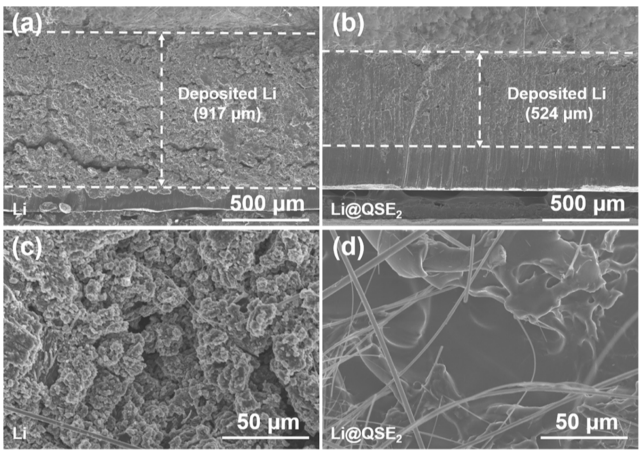

Figure 6. SEM images of Li anodes after 90 cycles. Cross-section morphology of (a) Li anode and (b) Li@QSE_2 anode. The surface morphology of (c) Li anode and (d) Li@QSE_2 anode.

In order to further optimize the interface between QSE and electrodes, LOBs were assembled with in situ formed QSE_2. The charge overpotential of LOB with in situ formed QSE_2 is comparable to the counterpart with LE, much lower than that with QSE_2 prepared with common procedures (Figure 7a–c). Furthermore, it increases in a slow rate, indicating the formation of a stable interface. The polarization data after the 10th cycle are shown in Table S3. A smaller polarization voltage is observed in the LOB with in situ formed QSE_2, which is very close to that of the LOB with LE. The in situ strategy has integrated the QSE and electrodes to an integrity, which is helpful for decreasing the interface polarization and constructing a more stable interface. Based on the strategy of in situ forming QSE in LOBs, lithium–oxygen pouch cell was assembled, as shown in Figure 7d. The pouch cell exhibits a discharge capacity of up to 17 520 mA h g^{-1} and a charge capacity of 16 515 mA h g^{-1} (Figure S25), which is competitive compared to other pouch cells reported in the literature, as shown in Table S4. The pouch cell can light up the LED lamp arrays (Figure 7e). Benefiting from the integrity of electrodes and QSE, it can still work well when folded. Even if a corner has been cut off, the LED lamp arrays can still shine very well, indicating good advantages of the QSE_2 in LOB, especially the in situ formed QSE_2.

4. CONCLUSIONS

In summary, a quasi-solid electrolyte membrane has been developed for LOBs, which has high ionic conductivity, excellent flexibility, and a wide electrochemical window. QSE can prevent O_2 and H_2O diffusing to the Li metal anode, and QSLOB is leakage free. QSLOBs with QSE_2 can run 317 cycles, showing a much better cycle performance than those with LE. QSE_2 can stabilize the interface layer on the cathode by reducing accumulation of decomposed byproducts, and it is supposed that the quasi-solid structure of QSE_2 can increase the number of TPBs on the cathode and promote the interfacial reaction of Li^+, electrons, and O_2. QSE_2 can act as an artificial interface layer to protect the Li metal anode by homogenizing Li^+ flux to promote uniform Li deposition. The results manifest that the developed QSE_2 can stabilize the interface of cathode and protect the Li metal anode to improve the cycle performance of LOBs. With in situ formed QSE_2, the electrodes can be combined to an integrity, further decreasing the interface polarization and constructing a more stable interface. Moreover, a lithium–oxygen pouch cell with in situ formed QSE_2 shows high stability when the cell was folded or even a corner was cut off. The QSE plays important roles both in the cathode and Li metal anode, which can be further improved with the in situ forming strategy, paving new ways to promote the performance of LOBs from multiple perspectives.

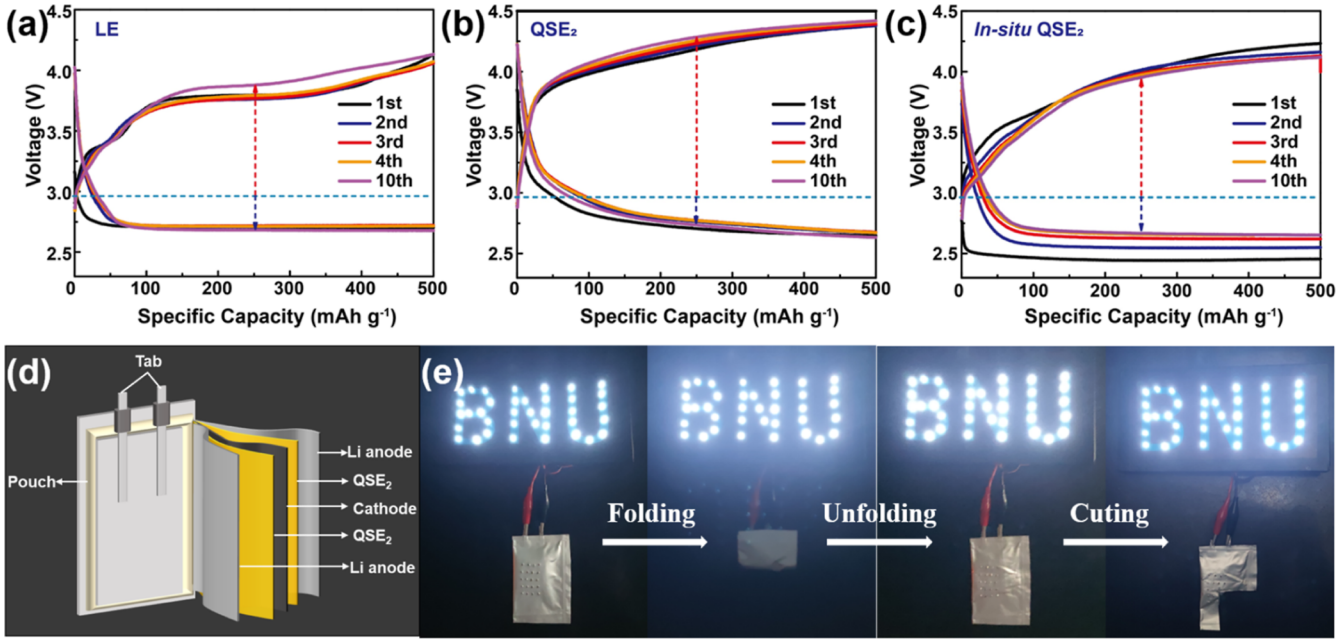

Figure 7. Selected discharge–charge curves of (a) LOB with LE, (b) LOB with QSE_2, and (c) LOB with in situ formed QSE_2. (d) Schematic illustration of the Li–O_2 pouch cell with in situ formed QSE_2 and (e) Powering the LED lamp arrays with the pouch cell.

https://doi.org/10.1021/acsomega.3c02917
ACS Omega 2023, 8, 36710–36719

■ ASSOCIATED CONTENT

Supporting Information

The Supporting Information is available free of charge at https://pubs.acs.org/doi/10.1021/acsomega.3c02917.

SEM images of cathode and Ru-MOF; XRD patterns of Ru-MOF and annealing Ru-MOF; EDS mapping of the cathode; ^{1}H NMR spectra of FG600; XRD profiles of QSE_2; DSC curves and T_g curves of cross-linked FG600 and QSE_2; DC polarization and EIS curves of LE and QSEs for determining the Li^+ transference number; FTIR spectra of the carbonyl groups in QSE_2; Raman spectra of $TFSI^-$ ions and ether bonds; TGA curves of QSEs and LE; leakage test of batteries; EIS curves and fitting results of Li|QSEs|O_2 batteries; XRD profiles of the pristine cathode, discharged and recharged cathodes; H_2O permeation experiments; XRD patterns of the Li anode; SEM images of Li@QSE_2; the cycling stability of Li−Li cell; selected discharge−charge curves of Li|LE|O_2 and Li@QSE_2|LE|O_2; cycle performance at 500 mA g^{-1} and 1000 mA h g^{-1}; CV profiles of the Li@QSE_2|LE|O_2; first five full discharge−charge curves of Li|LE|O_2 and Li@QSE_2|LE|O_2; EIS curves of Li|LE|O_2 and Li@QSE_2|LE|O_2; the performance comparison of the polymer electrolytes and LOBs; EIS fitting results of Li|LE|O_2 and QSE_2@Li|LE|O_2 at various stages; comparison of voltage values in the 10th cycle for Li|LE|O_2, in situ Li|QSE_2|O_2 and ex situ Li|QSE_2|O_2 batteries; and comparison of the Li−O_2 pouch cell (PDF)

■ AUTHOR INFORMATION

Corresponding Authors

FengQuan Liu − *College of Textiles & Clothing, Qingdao University, Qingdao 266071, China*; Email: fqliu@qdu.edu.cn

JianJun Zhou − *Beijing Key Laboratory of Energy Conversion and Storage Materials, College of Chemistry, Beijing Normal University, Beijing 100875, China*; Email: pla_zjj@bnu.edu.cn

Lin Li − *Beijing Key Laboratory of Energy Conversion and Storage Materials, College of Chemistry, Beijing Normal University, Beijing 100875, China; College of Textiles & Clothing, Qingdao University, Qingdao 266071, China*; orcid.org/0000-0002-2444-6694; Email: lilinll@bnu.edu.cn

Authors

SiXin Jia − *Beijing Key Laboratory of Energy Conversion and Storage Materials, College of Chemistry, Beijing Normal University, Beijing 100875, China*

JinXin Xue − *Beijing Key Laboratory of Energy Conversion and Storage Materials, College of Chemistry, Beijing Normal University, Beijing 100875, China*

Rui Wang − *Beijing Key Laboratory of Energy Conversion and Storage Materials, College of Chemistry, Beijing Normal University, Beijing 100875, China*

Hong Huo − *Beijing Key Laboratory of Energy Conversion and Storage Materials, College of Chemistry, Beijing Normal University, Beijing 100875, China*; orcid.org/0000-0002-1434-4475

Complete contact information is available at: https://pubs.acs.org/10.1021/acsomega.3c02917

Notes

The authors declare no competing financial interest.

■ ACKNOWLEDGMENTS

The authors appreciate the supporting of Natural Science Foundation of China (grant no. 21973008, 22179010, and 22109079).

■ REFERENCES

(1) Lu, Y. C.; Gallant, B. M.; Kwabi, D. G.; Harding, J. R.; Mitchell, R. R.; Whittingham, M. S.; Shao-Horn, Y. Lithium-Oxygen Batteries: Bridging Mechanistic Understanding and Battery Performance. *Energy Environ. Sci.* **2013**, *6*, 750.

(2) Chi, X. W.; Li, M. L.; Di, J. C.; Bai, P.; Song, L. N.; Wang, X. X.; Li, F.; Liang, S.; Xu, J. J.; Yu, J. H. A Highly Stable and Flexible Zeolite Electrolyte Solid-State Li-Air Battery. *Nature* **2021**, *592*, 551−557.

(3) Lu, J.; Li, L.; Park, J. B.; Sun, Y. K.; Wu, F.; Amine, K. Aprotic and Aqueous Li-O_2 Batteries. *Chem. Rev.* **2014**, *114*, 5611−5640.

(4) Liu, J.; Bao, Z. N.; Cui, Y.; Dufek, E. J.; Goodenough, J. B.; Khalifah, P.; Li, Q. Y.; Liaw, B. Y.; Liu, P.; Manthiram, A.; Meng, Y. S.; Subramanian, V. R.; Toney, M. F.; Viswanathan, V. V.; Whittingham, M. S.; Xiao, J.; Xu, W.; Yang, J.; Yang, X. Q.; Zhang, J. G. Pathways for Practical High-Energy Long-Cycling Lithium Metal Batteries. *Nat. Energy* **2019**, *4*, 180−186.

(5) He, Y.; Su, Y. H.; Qin, Y. Z.; Ding, L. Y.; Li, X.; Mei, S. W.; Zhang, Y. Z.; Ma, Y.; Wei, L.; Gu, Y. T.; Peng, Y.; Deng, Z. Stepping Up the Kinetics of Li-O_2 Batteries by Shrinking Down the Li_2O_2 Granules Through Concertedly Enhanced Catalytic Activity and Photoactivity of Se-Doped $LaCoO_3$. *ACS Appl. Mater. Interfaces* **2023**, *15*, 9285−9295.

(6) Li, F.; Zhang, T.; Zhou, H. S. Challenges of Non-Aqueous Li-O_2 Batteries: Electrolytes, Catalysts, and Anodes. *Energy Environ. Sci.* **2013**, *6*, 1125−1141.

(7) Ahmed, G.; Awan, Z. u. H.; Butt, F. A.; Raza, F.; Hashmi, S.; Gnana Kumar, G.; Christy, M. The Study of Different Redox Mediators for Competent Li-Air Batteries. *J. Power Sources* **2022**, *538*, 231379.

(8) Wang, X. X.; Guan, D. H.; Li, F.; Li, M. L.; Zheng, L. J.; Xu, J. J. Magnetic and Optical Field Multi-Assisted Li-O_2 Batteries with Ultrahigh Energy Efficiency and Cycle Stability. *Adv. Mater.* **2022**, *34*, No. e2104792.

(9) Zhao, L. Y.; Xing, Y.; Chen, N.; Lai, J. N.; Li, L.; Wu, F.; Chen, R. J. A Robust Cathode of RuO_2 nH_2O Clusters Anchored on the Carbon Nanofibers for Ultralong-Life Lithium-Oxygen Batteries. *J. Power Sources* **2020**, *463*, 228161.

(10) Bruce, P. G.; Freunberger, S. A.; Hardwick, L. J.; Tarascon, J. M. Li-O_2 and Li-S Batteries with High Energy Storage. *Nat. Mater.* **2012**, *11*, 19−29.

(11) Xu, Z. L.; Liu, Z. Q.; Gu, Z.; Zhao, X. L.; Guo, D. C.; Yao, X. Y. Polyimide-Based Solid-State Gel Polymer Electrolyte for Lithium-Oxygen Batteries with a Long-Cycling Life. *ACS Appl. Mater. Interfaces* **2023**, *15*, 7014−7022.

(12) Wang, X. X.; Guan, D. H.; Miao, C. L.; Kong, D. C.; Zheng, L. J.; Xu, J. J. Metal-Organic Framework-Based Mixed Conductors Achieve Highly Stable Photo-Assisted Solid-State Lithium-Oxygen Batteries. *J. Am. Chem. Soc.* **2023**, *145*, 5718−5729.

(13) Black, R.; Adams, B.; Nazar, L. F. Non-Aqueous and Hybrid Li-O_2 Batteries. *Adv. Energy Mater.* **2012**, *2*, 801−815.

(14) Yin, Y. B.; Yang, X. Y.; Chang, Z. W.; Zhu, Y. H.; Liu, T.; Yan, J. M.; Jiang, Q. A Water-/Fireproof Flexible Lithium-Oxygen Battery Achieved by Synergy of Novel Architecture and Multifunctional Separator. *Adv. Mater.* **2018**, *30*, 1703791.

(15) Yi, J.; Guo, S. H.; He, P.; Zhou, H. S. Status and Prospects of Polymer Electrolytes for Solid-State Li-O_2 (Air) Batteries. *Energy Environ. Sci.* **2017**, *10*, 860−884.

(16) Liu, Q. C.; Liu, T.; Liu, D. P.; Li, Z. J.; Zhang, X. B.; Zhang, Y. A Flexible and Wearable Lithium-Oxygen Battery with Record Energy

Density Achieved by the Interlaced Architecture Inspired by Bamboo Slips. *Adv. Mater.* **2016**, *28*, 8413−8418.
(17) Gao, K. N.; Wang, H. R.; He, M. H.; Li, Y. Q.; Cui, Z. H.; Mao, Y.; Zhang, T. Interfacial Integration and Roll Forming of Quasi-Solid-State Li-O_2 Battery Through Solidification and Gelation of Ionic Liquid. *J. Power Sources* **2020**, *463*, 228179.
(18) Le Bideau, J.; Viau, L.; Vioux, A. Ionogels, Ionic Liquid Based Hybrid Materials. *Chem. Soc. Rev.* **2011**, *40*, 907−925.
(19) Long, L. Z.; Wang, S. J.; Xiao, M.; Meng, Y. Z. Polymer Electrolytes for Lithium Polymer Batteries. *J. Mater. Chem. A* **2016**, *4*, 10038−10069.
(20) Xue, Z. G.; He, D.; Xie, X. L. Poly(ethylene oxide)-Based Electrolytes for Lithium-Ion Batteries. *J. Mater. Chem. A* **2015**, *3*, 19218−19253.
(21) Lei, J.; Gao, Z. Y.; Tang, L. B.; Zhong, L.; Li, J. J.; Zhang, Y.; Liu, T. Coupling Water-Proof Li Anodes with LiOH-Based Cathodes Enables Highly Rechargeable Lithium-Air Batteries Operating in Ambient Air. *Adv. Sci.* **2022**, *9*, No. e2103760.
(22) Celik, M.; Kızılaslan, A.; Can, M.; Cetinkaya, T.; Akbulut, H. Electrochemical Investigation of PVDF: HFP Gel Polymer Electrolytes for Quasi-Solid-State Li-O_2 Batteries: Effect of Lithium Salt Type and Concentration. *Electrochim. Acta* **2021**, *371*, 137824.
(23) Kang, G. D.; Cao, Y. M. Application and Modification of Poly(vinylidene fluoride) (PVDF) Membranes-A Review. *J. Membr. Sci.* **2014**, *463*, 145−165.
(24) Kim, Y. B.; Kim, I. T.; Song, M. J.; Shin, M. W. Synthesis of a Polyacrylonitrile/Tetrachloro-1,4-benzoquinone Gel Polymer Electrolyte for High-Performance Li-Air Batteries. *J. Membr. Sci.* **2018**, *563*, 835−842.
(25) Manuel Stephan, A. Review on Gel Polymer Electrolytes for Lithium Batteries. *Eur. Polym. J.* **2006**, *42*, 21−42.
(26) Zhao, H. M.; Liu, X. Q.; Chi, Z. Z.; Chen, S. X.; Li, S. X.; Guo, Z. Y.; Wang, L. Designing a New-Type PMMA Based Gel Polymer Electrolyte Incorporating Ionic Liquid for Lithium Oxygen Batteries with Ru-Based Binder-Free Cathode. *Appl. Surf. Sci.* **2021**, *565*, 150612.
(27) Wang, W. H.; Su, W.; Hu, S. Y.; Huang, Y.; Pan, Y.; Chang, S. C.; Shu, C. M. Pyrolysis Characteristics and Kinetics of Polymethylmethacrylate-Based Polymer Electrolytes for Lithium-Ion Battery. *J. Therm. Anal. Calorim.* **2022**, *147*, 12019−12032.
(28) Wang, H. F.; Wang, X. X.; Li, F.; Xu, J. J. Fundamental Understanding and Construction of Solid-State Li-Air Batteries. *Small Sci.* **2022**, *2*, 2200005.
(29) Freunberger, S. A.; Chen, Y.; Peng, Z.; Griffin, J. M.; Hardwick, L. J.; Barde, F.; Novak, P.; Bruce, P. G. Reactions in the Rechargeable Lithium-O_2 Battery with Alkyl Carbonate Electrolytes. *J. Am. Chem. Soc.* **2011**, *133*, 8040−8047.
(30) Girishkumar, G.; McCloskey, B.; Luntz, A. C.; Swanson, S.; Wilcke, W. Lithium-Air Battery: Promise and Challenges. *J. Phys. Chem. Lett.* **2010**, *1*, 2193−2203.
(31) Zhang, J. Q.; Sun, B.; Xie, X. Q.; Kretschmer, K.; Wang, G. X. Enhancement of Stability for Lithium Oxygen Batteries by Employing Electrolytes Gelled by Poly(vinylidene fluoride-co-hexafluoropropylene) and Tetraethylene Glycol Dimethyl Ether. *Electrochim. Acta* **2015**, *183*, 56−62.
(32) Shu, C. Z.; Long, J. P.; Dou, S. X.; Wang, J. Z. Component-Interaction Reinforced Quasi-Solid Electrolyte with Multifunctionality for Flexible Li-O_2 Battery with Superior Safety under Extreme Conditions. *Small* **2019**, *15*, No. e1804701.
(33) Cho, S. M.; Shim, J.; Cho, S. H.; Kim, J.; Son, B. D.; Lee, J. C.; Yoon, W. Y. Quasi-Solid-State Rechargeable Li-O_2 Batteries with High Safety and Long Cycle Life at Room Temperature. *ACS Appl. Mater. Interfaces* **2018**, *10*, 15634−15641.
(34) Zou, X. H.; Lu, Q.; Zhong, Y. J.; Liao, K. M.; Zhou, W.; Shao, Z. P. Flexible, Flame-Resistant, and Dendrite-Impermeable Gel-Polymer Electrolyte for Li-O_2/Air Batteries Workable Under Hurdle Conditions. *Small* **2018**, *14*, No. e1801798.
(35) Amici, J.; Alidoost, M.; Caldera, F.; Versaci, D.; Zubair, U.; Trotta, F.; Francia, C.; Bodoardo, S. PEEK-WC/Nanosponge Membranes for Lithium-Anode Protection in Rechargeable Li-O_2 Batteries. *ChemElectroChem* **2018**, *5*, 1599−1605.
(36) Liu, T.; Liu, Q. C.; Xu, J. J.; Zhang, X. B. Cable-Type Water-Survivable Flexible Li-O_2 Battery. *Small* **2016**, *12*, 3101−3105.
(37) Liu, F. Q.; Bin, F. J.; Xue, J. X.; Wang, L.; Yang, Y. J.; Huo, H.; Zhou, J. J.; Li, L. Polymer Electrolyte Membrane with High Ionic Conductivity and Enhanced Interfacial Stability for Lithium Metal Battery. *ACS Appl. Mater. Interfaces* **2020**, *12*, 22710−22720.
(38) Meng, X. K.; Liao, K. M.; Dai, J.; Zou, X. H.; She, S. X.; Zhou, W.; Ye, F.; Shao, Z. P. Ultralong Cycle Life Li-O_2 Battery Enabled by a MOF-Derived Ruthenium-Carbon Composite Catalyst with a Durable Regenerative Surface. *ACS Appl. Mater. Interfaces* **2019**, *11*, 20091−20097.
(39) Kwak, W. J.; Park, J.; Nguyen, T. T.; Kim, H.; Byon, H. R.; Jang, M.; Sun, Y. K. A Dendrite- and Oxygen-Proof Protective Layer for Lithium Metal in Lithium-Oxygen Batteries. *J. Mater. Chem. A* **2019**, *7*, 3857−3862.
(40) Lyu, Z. Y.; Zhou, Y.; Dai, W. R.; Cui, X. H.; Lai, M.; Wang, L.; Huo, F. W.; Huang, W.; Hu, Z.; Chen, W. Recent Advances in Understanding of the Mechanism and Control of Li_2O_2 Formation in Aprotic Li-O_2 Batteries. *Chem. Soc. Rev.* **2017**, *46*, 6046−6072.
(41) Xu, J. J.; Chang, Z. W.; Wang, Y.; Liu, D. P.; Zhang, Y.; Zhang, X. B. Cathode Surface-Induced, Solvation-Mediated, Micrometer-Sized Li_2O_2 Cycling for Li-O_2 Batteries. *Adv. Mater.* **2016**, *28*, 9620−9628.
(42) Kwabi, D. G.; Tulodziecki, M.; Pour, N.; Itkis, D. M.; Thompson, C. V.; Shao-Horn, Y. Controlling Solution-Mediated Reaction Mechanisms of Oxygen Reduction Using Potential and Solvent for Aprotic Lithium-Oxygen Batteries. *J. Phys. Chem. Lett.* **2016**, *7*, 1204−1212.
(43) Adams, B. D.; Radtke, C.; Black, R.; Trudeau, M. L.; Zaghib, K.; Nazar, L. F. Current Density Dependence of Peroxide Formation in the Li-O_2 Battery and its Effect on Charge. *Energy Environ. Sci.* **2013**, *6*, 1772.
(44) Wang, X. X.; Chi, X. W.; Li, M. L.; Guan, D. H.; Miao, C. L.; Xu, J. J. An Integrated Solid-State Lithium-Oxygen Battery with Highly Stable Anionic Covalent Organic Frameworks Electrolyte. *Chem* **2023**, *9*, 394−410.
(45) Wang, X. X.; Gan, S. C.; Zheng, L. J.; Li, M. L.; Xu, J. J. Bioinspired Fabrication of Strong Self-Standing Egg-Sugarcane Cathodes for Rechargeable Lithium-Oxygen Batteries. *CCS Chem.* **2021**, *3*, 1764−1774.
(46) Song, S. D.; Zhang, D. Q.; Ruan, Y. L.; Yu, L. M.; Xu, Y. Q.; Thokchom, J.; Mei, D. H. Quasi-Solid-State Li-O_2 Batteries Performance Enhancement Using an Integrated Composite Polymer-Based Architecture. *ACS Appl. Energy Mater.* **2021**, *4*, 6221−6232.
(47) Freunberger, S. A.; Chen, Y.; Drewett, N. E.; Hardwick, L. J.; Barde, F.; Bruce, P. G. The Lithium-Oxygen Battery with Ether-Based Electrolytes. *Angew. Chem. Int. Ed.* **2011**, *50*, 8609−8613.
(48) Ottakam Thotiyl, M. M.; Freunberger, S. A.; Peng, Z.; Bruce, P. G. The Carbon Electrode in Nonaqueous Li-O_2 Cells. *J. Am. Chem. Soc.* **2013**, *135*, 494−500.
(49) Cao, D.; Bai, Y.; Zhang, J.; Tan, G.; Wu, C. Irreplaceable Carbon Boosts Li-O_2 Batteries: From Mechanism Research to Practical Application. *Nano Energy* **2021**, *89*, 106464.
(50) Liu, Q. C.; Xu, J. J.; Yuan, S.; Chang, Z. W.; Xu, D.; Yin, Y. B.; Li, L.; Zhong, H. X.; Jiang, Y. S.; Yan, J. M.; Zhang, X. B. Artificial Protection Film on Lithium Metal Anode toward Long-Cycle-Life Lithium-Oxygen Batteries. *Adv. Mater.* **2015**, *27*, 5241−5247.
(51) Chen, W. X.; Luo, Z. H.; Zhuge, X. Q.; Ding, Z. P.; Ren, Y. R.; Loya, A.; Li, Y.; Luo, K. Protecting Lithium Anode with Ionic Liquid Modified Poly(vinylidene fluoride) Single Ion Conducting Separators for Iodide-Assisted Lithium Oxygen Batteries. *J. Energy Storage* **2022**, *50*, 104580.
(52) Zhang, G. L.; Li, G. Y.; Wang, J.; Tong, H.; Wang, J.; Du, Y.; Sun, S. H.; Dang, F. 2D SnSe Cathode Catalyst Featuring an Efficient Facet-Dependent Selective Li_2O_2 Growth/Decomposition for Li-Oxygen Batteries. *Adv. Energy Mater.* **2022**, *12*, 2103910.

https://doi.org/10.1021/acsomega.3c02917
ACS Omega 2023, 8, 36710−36719

(53) Li, F.; Li, M. L.; Wang, H. F.; Wang, X. X.; Zheng, L. J.; Guan, D. H.; Chang, L. M.; Xu, J. J.; Wang, Y. Oxygen Vacancy-Mediated Growth of Amorphous Discharge Products toward an Ultrawide Band Light-Assisted Li-O_2 Batteries. *Adv. Mater.* **2022**, *34*, No. e2107826.
(54) Ju, B.; Song, H. J.; Lee, G. H.; Sung, M. C.; Kim, D. W. Nickel Disulfide Nanosheet as Promising Cathode Electrocatalyst for Long-Life Lithium-Oxygen Batteries. *Energy Storage Mater.* **2020**, *24*, 594−601.
(55) Zhang, W. X.; Tang, S.; Chen, Z. H.; Xiong, X. C.; Chen, B.; Wu, K.; Xu, G. H.; Cheng, S. J.; Cao, Y. C. The Controllable Construction of Nanochannel in Two-Dimensional Lamellar Film for Efficient Oxygen Reduction Reaction and Lithium-Oxygen Batteries. *Chem. Eng. J.* **2022**, *430*, 132489.
(56) Qiao, Y.; He, Y. B.; Wu, S. C.; Jiang, K. Z.; Li, X.; Guo, S. H.; He, P.; Zhou, H. S. MOF-Based Separator in a Li-O_2 Battery: An Effective Strategy to Restrain the Shuttling of Dual Redox Mediators. *ACS Energy Lett.* **2018**, *3*, 463−468.
(57) Zheng, L. J.; Bai, P.; Yan, W. F.; Li, F.; Wang, X. X.; Xu, J. J. In Situ Construction of Glass-fiber-directed Zeolite Microtube Woven Separator for Ultra-high-capacity Lithium-Oxygen Batteries. *Matter* **2023**, *6*, 142−157.
(58) Zhang, X.; Xie, Z. J.; Zhou, Z. Recent Progress in Protecting Lithium Anodes for Li-O_2 Batteries. *ChemElectroChem* **2019**, *6*, 1969−1977.
(59) Lee, D. J.; Lee, H.; Kim, Y. J.; Park, J. K.; Kim, H. T. Sustainable Redox Mediation for Lithium-Oxygen Batteries by a Composite Protective Layer on the Lithium-Metal Anode. *Adv. Mater.* **2016**, *28*, 857−863.
(60) Cheng, X. B.; Zhang, R.; Zhao, C. Z.; Wei, F.; Zhang, J. G.; Zhang, Q. A Review of Solid Electrolyte Interphases on Lithium Metal Anode. *Adv. Sci.* **2016**, *3*, 1500213.

https://doi.org/10.1021/acsomega.3c02917
ACS Omega 2023, 8, 36710−36719